NH$_2$-MIL-101(Fe)/Ni(OH)$_2$-derived C,N-codoped Fe$_2$P/Ni$_2$P cocatalyst modified g-C$_3$N$_4$ for enhanced photocatalytic hydrogen evolution from water splitting

Jixiang Xu, Yinhong Qi, Chao Wang, Lei Wang[*]

Key Laboratory of Eco-Chemical Engineering, Taishan Scholar Advantage and Characteristic Discipline Team of Eco Chemical Process and Technology, College of Chemistry and Molecular Engineering, Qingdao University of Science and Technology, Qingdao 266042, China

ARTICLE INFO

ABSTRACT

Constructing appropriate cocatalysts to modify semiconductors while maintaining tight interface for charge separation facilitation is important for improving photocatalytic hydrogen production. Thus, in this work, C,N-codoped Fe$_2$P/Ni$_2$P (CN/FeNiP) polyhedrons derived from NH$_2$-MIL-101(Fe)/Ni(OH)$_2$ were used as cocatalysts to modify graphitic carbon nitride (g-C$_3$N$_4$) for photocatalytic hydrogen production from water splitting under visible-light irradiation. The highest evolution rate observed over CN/FeNiP/g-C$_3$N$_4$ was 13.81 mmol g^{-1} h^{-1} under 1.0 mmol L^{-1} of Eosin Y (EY) sensitization (compared to 0.196 mmol g^{-1} h^{-1} without EY sensitization), which was about 10 and 5 times higher than that of g-C$_3$N$_4$ (1.33 mmol g^{-1} h^{-1}) and CN/FeP/g-C$_3$N$_4$ (2.73 mmol g^{-1} h^{-1}). The apparent quantum yield at 420 nm reached 45.8%. A detail analysis of the mechanism revealed that the improved photocatalytic activity can be ascribed to highly efficient spatial separation of photo-induced charges from the excited EY and g-C$_3$N$_4$ to CN/FeNiP with tight interface, staggered band energy between g-C$_3$N$_4$, CN/Fe$_2$P and Ni$_2$P as well as accelerated surface reaction by CN/FeNiP cocatalysts. This work demonstrates that MOF-derived hybrid hollow metal phosphide can be good substitutes for noble metal catalysts for photocatalytic hydrogen production.

1. Introduction

The sunlight driven evolution of hydrogen from water using semiconductors is a cheap and promising technology that converts solar to chemical energy and supports sustainable development [1,2]. To date, a large number of semiconductor-based photocatalysts, such as TiO$_2$, CdS, bimetallic sulfides, ZnO, g-C$_3$N$_4$, *etc.*, have been explored [3–19]. Among them, g-C$_3$N$_4$ with flexible layered structure is one of the most promising ones for hydrogen generation by water splitting under visible-light irradiation because of its relatively narrow band gap of ∼2.7 eV, suitable band edge positions and excellent durability [20]. However, the inherently fast recombination of photo-generated electron-hole pairs restricts its photocatalytic activity. An efficient strategy to solve this issue is to load suitable cocatalyst on g-C$_3$N$_4$ to provide abundant active sites, which could not only promote the charge separation efficiency, but also lower the activation potential of H$_2$ evolution reaction. Noble metals, such as Pt, Ag, and Au, were used as efficient cocatalysts to enhance photocatalytic performance of g-C$_3$N$_4$ [21–23]. However, noble metals are too expensive for practical

applications in catalysis. Thus, some low-cost metal sulfides and transition metal phosphides, including CoP, FeP, MoP, Cu$_3$P, Ni$_2$P and RhP, were developed as ideal substitutes of noble metals to promote photocatalytic H$_2$ generation [24–38]. Among them, FeP is especially attractive for the electrochemical hydrogen evolution reaction (HER) because of its more negative conduction band (−0.059 V versus normal hydrogen electrode (NHE) at pH 1.0) and low cost. Some works reported using FeP as a cocatalyst for photocatalytic H$_2$ generation [39–42]. Bimetallic phosphides offer enhanced charge transfer between different ions and effectively modulate their 3d electronic structures, resulting in dramatically enhanced HER activity [43]. NiCoP is such example as it was used for photocatalytic H$_2$ evolution [44–46]. Some researches were done on NiFeP for electrocatalytic H$_2$ evolution or water oxidation [47–49], however, utilization of NiFeP as a cocatalyst decorated with g-C$_3$N$_4$ for hydrogen evolution by water splitting has not been reported to our knowledge.

To improve spectral responsive capability and to further enhance photocatalytic activity of g-C$_3$N$_4$, dye sensitization is also an effective approach. In this kind of systems, developing an excellent cocatalyst

---

* Corresponding author.
  E-mail address: inorchemwl@126.com (L. Wang).

acting as an electron trap center to accelerate the electron transfer from the excited dye molecules to the active sites and to suppress the reverse electron transfer of LUMO state electrons to HOMO states of dye molecule are required. Most of the reported cocatalysts are noble metals (especially Pt), the main drawbacks of which are their high price and scarcity. Therefore, some non-precious cocatalysts such as $Ni(OH)_2$, $Ni@NiO$, NiS_x/graphene, CuO, CuO/Cr_2O_3, $Co@CoS$ and MoS_2/graphene were developed to facilitate electron transfer [50,51]. Among noble metal-free cocatalysts, transition metal phosphides were used as an earth-abundant cocatalyst to capture photo-induced charges in non-dye sensitized systems [24–31], but the capability of these metal phosphides to transfer electron from the excited dye to the active sites was less investigated.

Design of the microstructure and morphology of metal phosphides to maximize their accessible active sites also has great influence on the catalytic performance of a semiconductor. In this regard, metal phosphides with hollow polyhedral structures are particularly attractive because of their large surface area, open surface structure and short charge transfer distance, all of which are beneficial for the photocatalytic H_2 evolution [37].

Hollow structures can generally be fabricated by a templating method. Metal–organic frameworks (MOFs), a family of crystalline porous materials with high surface area, well-designed structure and morphology, show great potential as templates for the *in situ* synthesis of hollow metal phosphide by phosphidation [43,52–54]. It was also used as host matrices for anchoring g-C_3N_4 to fabricate MOF/g-C_3N_4 composite with improved photocatalytic performance and very efficient interfacial charge transfer. Among different MOFs, NH_2-MIL-101(Fe), a Fe-containing MOF composed of iron oxo-clusters and amino-terephthalates, can be used as both sacrificial templates and metal precursors to prepare FeP polyhedrons with many exposed edges and surface active sites. On the other hand, the high surface area makes it an ideal support to stabilize nanoparticle and to prevent their aggregation as well as to anchor g-C_3N_4 to fabricate g-C_3N_4-based composite with tight contact interface for fast charge transport.

Taking all this into account, we developed a novel approach for enhancing photocatalytic H_2 evolution performance of g-C_3N_4 using C,N-codoped Fe_2P/Ni_2P (CN/FeNiP) polyhedrons as cocatalyst. First, NH_2-MIL-101(Fe) was used as a matrix to anchor $Ni(OH)_2$ nanoparticles, and then g-C_3N_4 nanosheets were deposited on the surface of NH_2-MIL-101(Fe)/$Ni(OH)_2$. Finally, the NH_2-MIL-101(Fe)/$Ni(OH)_2$/g-C_3N_4 was phosphidized. During the annealing of NH_2-MIL-101(Fe)/$Ni(OH)_2$/g-C_3N_4 composite, CN/FeNiP polyhedrons formed tight interfaces with g-C_3N_4 necessarily for rapid photo-generated charge separation. Combination of hollow polyhedral structure and synergistic effect of the second metal provides as-obtained CN/FeNiP catalysts with excellent activity relative to g-C_3N_4 for H_2 evolution under visible-light irradiation. Compared to unmodified g-C_3N_4, CN/FeP/g-C_3N_4, simple physical mixture of CN/FeNiP and g-C_3N_4, CN/FeNi$_{7.47}$P/g-C_3N_4 composite exhibited higher H_2 evolution rate equal to 13.81 mmol h^{-1} g^{-1} under 1.0 mmol L^{-1} Eosin Y (EY)-sensitization, which is 10 times higher than that for unmodified g-C_3N_4. We also propose mechanism of the improved H_2 evolution performance of the CN/FeNiP/g-C_3N_4 composite.

2. Experimental

2.1. Preparation of CN/FeNiP/g-C_3N_4 composites

$Ni(OH)_2$ nanoparticles were synthesized by a hydrothermal method. NH_2-MIL-101(Fe) was synthesized using a solvothermal method reported elsewhere [55]. g-C_3N_4 was obtained by thermal treatment of melamine precursor. Details for experimental procedures for $Ni(OH)_2$, NH_2-MIL-101(Fe) and g-C_3N_4 syntheses are provided in the Supplementary Materials.

For the preparation of NH_2-MIL-101(Fe)/$Ni(OH)_2$/g-C_3N_4 composites, different amounts of $Ni(OH)_2$ (10, 20, 30, 40 and 50 mg) and 50 mg of NH_2-MIL-101(Fe) were dispersed (in separate flasks) in 10 mL of methanol by ultrasonication for 10 min. Then the $Ni(OH)_2$ suspension was added into the NH_2-MIL-101(Fe) suspension, stirred at ambient temperature for 2 h and finally collected by centrifugation. Then the product was washed with methanol and dispersed in 10 mL of 10 g L^{-1} g-C_3N_4 methanol suspension with constant stirring at 60 °C for 24 h. The NH_2-MIL-101(Fe)/$Ni(OH)_2$/g-C_3N_4 precursor was obtained by evaporating methanol from this suspension.

Using NH_2-MIL-101(Fe)/$Ni(OH)_2$/g-C_3N_4 obtained as described above as a sacrificial template, bimetallic phosphide modified with g-C_3N_4 were synthesized by annealing. In a typical process, NH_2-MIL-101(Fe)/$Ni(OH)_2$/g-C_3N_4 and NaH_2PO_2 with optimal mass ratio of 1:5 were placed at two separate positions (downstream and upstream, respectively) of the same quartz tube under constant N_2 flow (shown in Fig. S1). Then the quartz tube was heated to the ideal temperature of 350 °C at a 5 °C min^{-1} heating rate and held at this temperature for 3 h followed by naturally cooling it to room temperature. The resulting black powder contained C (56.48%), N (3.05%), Fe (27.88%), Ni (0.13%), P (12.11%) and Na (0.35%) (Fig. S2) according to the energy dispersive spectroscopy (EDS). This sample was denoted as CN/FeNiP/g-C_3N_4. It was then loaded with 2.65, 4.25, 6.71, 7.47 and 11.37% of Ni_2P, which was confirmed by ICP-OMS measurements. Samples with different amounts of Ni_2P were labeled according to the percentage of the Ni_2P content, namely, CN/FeNi$_{2.65}$P/g-C_3N_4, CN/FeNi$_{4.25}$P/g-C_3N_4, CN/FeNi$_{6.71}$P/g-C_3N_4, CN/FeNi$_{7.47}$P/g-C_3N_4 and CN/FeNi$_{11.37}$P/g-C_3N_4. CN/FeP/g-C_3N_4 sample was also prepared using the similar procedure but without addition of $Ni(OH)_2$.

2.2. Characterization

Powder X-ray diffraction (XRD) data were collected using a Rigaku D–MAX 2500/PC diffractometer equipped with a Cu Kα radiation source. X-ray photoelectron spectra (XPS) were recorded using an X-ray photoelectron spectrometer (Thermo Scientific, Kα) equipped with a monochromatic Al Ka X-ray source (hν = 1486.6 eV). UV–vis diffuse reflectance spectra were recorded using a Lambda 750 UV/VIS/NIR spectrometer. The morphology of the as-obtained samples was analyzed by scanning electron microscopy (SEM) using a TESCAN-VEGA3 instrument. High-resolution transmission electron microscopy (HR-TEM) images were obtained using a Tecnai-G^2-F30 high-resolution transmission electron microscope (FEI Company, USA). High-angle annular dark field scanning TEM (HAADF-STEM) coupled with energy dispersive spectroscopy (EDS) with elemental mapping capability was recorded by a Bruker super-X EDS. Fluor-spectrophotometer (F-4500 FL) was used to record photoluminescence (PL) spectra. The time resolved photoluminescence (TRPL) spectra were recorded on an Edinburgh FS5 fluorescence spectrofluorometer. The amounts of Ni_2P loaded on CN/FeNiP/g-C_3N_4 composites were analyzed using a Thermo ICAP-QC inductively coupled plasma optical emission spectroscopy (ICP-OMS). N_2 adsorption-desorption isotherms were measured by a Micromeritics ASAP 2020 apparatus at 77 K (Micromeritics, Norcross, GA, USA).

2.3. Photocatalytic activity for H_2 evolution

Photocatalytic reaction was carried out in a quartz flask equipped with a flat optical entry window. 10 mg of the photocatalyst was dispersed in 80 mL of aqueous solution containing 10% of triethanolamine (TEOA) (by volume) used as a sacrificial agent and 1 mmol L^{-1} of EY used as a photosensitizer. Different amounts of EY were added to study EY effect on H_2 evolution. The system was deaerated by bubbling N_2 into the solution for 10 min before irradiation. A 300-W Xe lamp with 420 nm cut-off filter was used as a visible-light source. The amount of H_2 evolved was determined at 1 h intervals using an online gas chromatography system (GC-7920). The apparent quantum efficiency (AQE) was measured under the same photocatalytic reaction conditions upon

irradiation using a 300-W Xe lamp with a 420 nm band pass filter. Photon flux of the incident light was determined using an optical power meter (CEL-NP2000, Beijing China Education Au-Light Co.). During the AQE test, the reaction mixtures were irradiated for 60 min. AQE was calculated using the following equation:

$$AQE = \frac{2 \times \text{the number of evolved hydrogen molecules}}{\text{the number of incident photons}} \times 100\%$$

2.4. Photoelectrochemical measurements

Photocurrent measurements and Mott–Schottky (MS) plots were obtained using a CHI 660D electrochemical workstation (Chenhua Instrument, Shanghai, China) in a conventional three-electrode configuration using a Pt foil as the counter electrode and Ag/AgCl (saturated with KCl) as the reference electrode. A 300-W Xe arc lamp (PLS-SXE300) was used as a light source. A 0.5 M Na_2SO_4 aqueous solution was used as electrolyte. The electrochemical impedance spectra (EIS) were recorded by the IM6e electrochemical station (Zahner Elektrik, Germany) using the same three-electrode system. To prepare the working electrodes, 5 mg of the photocatalyst was ground with 5 μL of acetylacetone and 500 μL of distilled water for 30 min. The resulting slurry was then spread on an ITO glass substrate with an active area of ~ 1 × 1 cm using a doctor-blade and an adhesive tape. The electrode was dried in air and annealed at 200 °C for 30 min under N_2 atmosphere.

3. Results and discussion

3.1. Catalyst characterization

XRD patterns of the g-C_3N_4, CN/FeP/g-C_3N_4, CN/FeNiP/g-C_3N_4 composites with various Ni_2P loadings are shown in Fig. 1. Pure g-C_3N_4 displayed two diffraction peaks at 2θ = 13.3° and 27.2°, corresponding to the (100) and (002) planes, respectively (see Fig. 1d) [56]. The main diffraction peaks of the as-synthesized NH_2-MIL-101(Fe) correspond to those reported previously (Fig. S3a) [55]. XRD peaks of CN/FeP/g-C_3N_4 appeared at 2θ angles equal to 29.7°, 34.0°, 44.0° and 52.9°, which correspond to the (101), (200), (201) and (002) planes of hexagonal Fe_2P (JCPDS No. 88-1803) [57]. No noticeable changes were observed at 2.65% Ni_2P loading (see Fig. 1b) due to the weak intensity of Ni_2P at this concentration. XRD pattern of CN/FeNiP was different than that of CN/Fe_2P (shown in Fig. S3c) since two new peaks at 26.2° and 57.4° of 2θ (corresponding to Ni_2P according to the JCPDS card No. 65-3544) were found in the XRD spectrum of CN/FeNiP (see Fig. S3b). These suggests that the loaded Ni(OH)$_2$ did not incorporate into the crystal lattice of NH_2-MIL-101(Fe) to form NiFeP solid solution. Because some

Fig. 1. XRD patterns of as-prepared (a) g-C_3N_4, (b) CN/FeP/g-C_3N_4, (c) CN/FeNi$_{2.65}$P/g-C_3N_4, (d) CN/FeNi$_{4.25}$P/g-C_3N_4 (e) CN/FeNi$_{6.71}$P/g-C_3N_4, (f) CN/FeNi$_{7.47}$P/g-C_3N_4 and (g) CN/FeNi$_{11.37}$P/g-C_3N_4 composites.

peaks of Ni_2P (JCPDS No. 65-3544) and Fe_2P (JCPDS No. 88-1803) overlap (Fig. S3b), it was hard to differentiate which exactly peaks belonged to Ni_2P and/or Fe_2P when analyzing peaks at 40.8, 47.2, and 54.2° that were observed at higher Ni_2P loading (4.25–11.37%). Moreover, peaks at 18.1° and 30.0° became more intense with increasing Ni_2P loading amounts. Additionally, at higher concentrations, characteristic peak of Ni_2P was detected at 32.7°.

XPS survey spectra confirmed presence of Ni, Fe, P, C and N elements. Chemical states of these elements were additionally studied by the high-resolution XPS. In the high-resolution Fe 2p spectrum (Fig. 2a), the binding energy (BE) peaks centered at 706.9 and 712.7 eV correspond to Fe 2p$_{3/2}$. Other signals centered at 719.5 and 725.0 eV can be assigned to Fe 2p$_{1/2}$. Peak at 706.9 eV belongs to Fe in Fe_2P, while the other two peaks at 712.7 and 719.5 eV can be assigned to oxidized Fe species [47,48]. BE peaks at 284.8 and 288.3 eV in the C 1 s spectrum (Fig. 2b) are from C—C and N—C = N bonds, respectively [58]. Peaks at 398.3, 399.5 and 401.0 eV in the N 1 s spectrum (Fig. 2c) can be assigned to the binding energies of C—N = C, N—(C)$_3$ and C—N—H from g-C_3N_4 [24]. In the Ni 2p spectrum (Fig. 2d), peaks located at 853.0 and 870.2 eV correspond to Niδ^+ in Ni_2P, and peaks at 856.2 and 874.3 eV can be assigned to oxidized Ni species (Ni^{2+}). Peak at 862.2 eV corresponds to the satellite of the Ni 2p$_{1/2}$ [46–48]. In the P 2p spectrum (shown in Fig. 2e), peak at 129.1 eV is characteristic of Pδ– bonds in metal phosphide, while the peak at 133.6 eV can be attributed to the oxidised P species due to the exposure to air [59]. Thus, XPS confirms XRD results about formation of CN/FeNiP/g-C_3N_4 composite.

Samples structures were also studied by FTIR (see Fig. S4). Absorption bands at 1243, 1318 and 1409 cm^{-1}, which could be attributed to the characteristic vibrations of C—NH—C units of g-C_3N_4, were distinctly observed in FTIR spectrum of CN/FeNi$_{7.47}$P/g-C_3N_4 [60]. Peak at 1080 cm^{-1} which can be assigned to the P=O stretching band and appeared because of the surface oxidation of Fe–P and Ni–P in air [61], was found in the CN/FeNi$_{7.47}$P/g-C_3N_4 spectrum. Relative intensity of this peak increased after loading Ni_2P onto CN/FeP/g-C_3N_4 (see Fig. S4a and b). These results indicated that Ni_2P and g-C_3N_4 were successfully combined with CN/Fe_2P.

Fig. 3 shows TEM images of NH_2-MIL-101(Fe), NH_2-MIL-101(Fe)/Ni(OH)$_2$ and CN/FeNi$_{7.47}$P/g-C_3N_4 composites. As-prepared NH_2-MIL-101(Fe) had hexagonal micro-spindle morphology with 700 nm long and 500 nm wide particles (Fig. 3a), which is also confirmed by SEM (Fig. S5a) [62]. Some black small particles of Ni(OH)$_2$ can be seen on the surface of NH_2-MIL-101(Fe) (Fig. 3b), indicating Ni(OH)$_2$ deposition. Figs. 3c and S5b shows TEM and SEM images of the CN/FeNi$_{7.47}$P/g-C_3N_4 composite. g-C_3N_4 was successfully coated on NH_2-MIL-101(Fe)-derived CN/Fe_2P and the contact interface is clearly visible. Fig. 3d shows clear lattice fringes with spacings equal to 0.22, 0.20 and 0.28 nm, which belong to the d-spacings of (111) and (201) planes of hexagonal Ni_2P and (111) plane of hexagonal Fe_2P [47,48], respectively, further indicating presence of Fe_2P and Ni_2P in the CN/FeNiP/g-C_3N_4 composite.

STEM-EDS elemental mapping of CN/FeNi$_{7.47}$P/g-C_3N_4 composite (shown in Fig. 4) further confirmed hexagonal morphology of obtained CN/Fe_2P. Distinct contact interfaces between g-C_3N_4 and CN/Fe_2P could be clearly seen. Ni_2P particles were deposited on the surface of the composite. Fe, Ni, P, N, and C were uniformly distributed in the structure of CN/FeNi$_{7.47}$P/g-C_3N_4.

The optical response properties of the as-prepared samples are displayed in Fig. 5. EY showed an obvious absorption in the 200–800 nm range (see Fig. 5i), while CN/Fe_2P showed low absorption in the same range (see Fig. 5a). Pure g-C_3N_4 showed an absorption band below ~460 nm, resulting in low visible-light utilization efficiency. After decorating g-C_3N_4 with CN/Fe_2P, CN/FeP/g-C_3N_4 composite showed enhanced visible-light absorption. After loading Ni(OH)$_2$ onto NH_2-MIL-101(Fe), the resulting CN/FeNiP/g-C_3N_4 composites showed almost the same absorption as CN/FeP/g-C_3N_4, but with higher absorption intensity, which increased with increasing loading amounts of
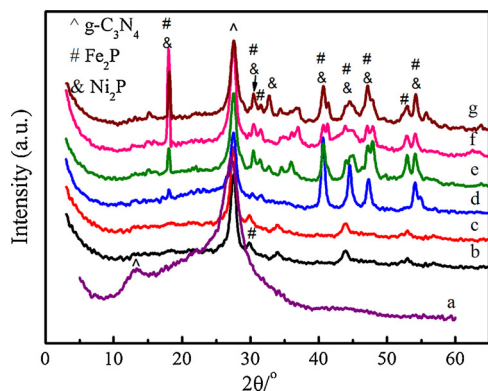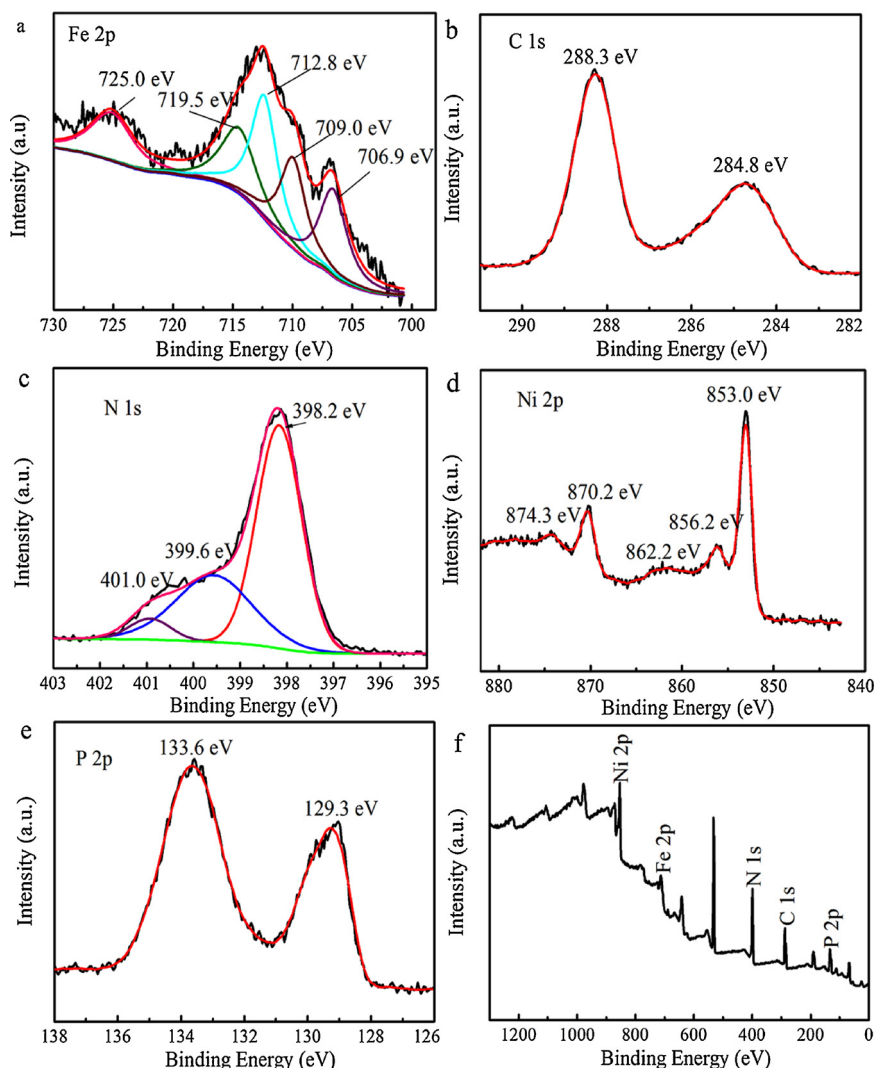
Fig. 2. XPS survey spectrum (f) of CN/FeNi$_{7.47}$P/g-C$_3$N$_4$ and high-resolution spectra of (a) Fe 2p, (b) C 1 s, (c) N 1 s, (d) Ni 2p and (e) P 2p.

Ni$_2$P.

3.2. Catalytic performance

Photocatalytic H$_2$ evolution of as-prepared samples was determined in the presence of 10% triethanolamine (TEOA), as a sacrificial agent for capturing holes, and 1.0 mmol L^{-1} of EY, as a photo-sensitizer (Fig. 6). Control experiment showed small amount of H$_2$ (1.33 mmol g^{-1} h^{-1}) when unmodified g-C$_3$N$_4$ was used. The rate of H$_2$ production over CN/Fe$_2$P-decorated g-C$_3$N$_4$ reached 2.73 mmol g^{-1} h^{-1}, double of that over g-C$_3$N$_4$. When 2.65% of Ni$_2$P was loaded on CN/Fe$_2$P to produce CN/FeNi$_{2.65}$P/g-C$_3$N$_4$ composite, H$_2$ evolution rate was 5.75 mmol g^{-1} h^{-1}. With the increasing loading amounts of Ni$_2$P, H$_2$ evolution rate increased as well. For CN/FeNi$_{4.25}$P/g-C$_3$N$_4$ and CN/FeNi$_{6.71}$P/g-C$_3$N$_4$, the H$_2$ evolution rates were 5.93 and 6.47 mmol g^{-1} h^{-1}, respectively. The highest photocatalytic H$_2$ evolution rate of 13.81 mmol g^{-1} h^{-1} was achieved with 7.47% of Ni$_2$P loading (CN/FeNi$_{7.47}$P/g-C$_3$N$_4$), which is approximately 5 times higher than that of Ni$_2$P-free CN/FeP/g-C$_3$N$_4$. The amount of H$_2$ evolved over CN/FeNi$_{7.47}$P/g-C$_3$N$_4$ during the 8 h experiment was 110.5 mmol g^{-1}, and the AQE of 48.5% was achieved at 420 nm. Further increase in the Ni$_2$P loading amount to 11.37% resulted in slight decrease of the H$_2$ evolution rate (to 13.63 mmol g^{-1} h^{-1}). We assume that excess of Ni$_2$P particles cover some of the active sites weakening the charge transport and hindering H$_2$ evolution [63]. In addition, H$_2$ evolution rate over

CN/FeNiP/g-C$_3$N$_4$ was influenced by EY concentration (Fig. S6). As shown in Fig. 6b, a very small amount of H$_2$ (0.196 mmol g^{-1} h^{-1}) was detected without EY-sensitization. Photocatalytic activity of CN/FeNi$_{7.47}$P/g-C$_3$N$_4$ was largely enhanced to 5.22 and 7.40 mmol g^{-1} h^{-1} when 0.1 and 0.5 mmol L^{-1} EY was added, respectively. Further increase in the EY concentration from 1.0 to 1.5 mmol L^{-1} led to the decrease of H$_2$ evolution rate from 13.81 to 9.39 mmol g^{-1} h^{-1} due to the self-quenching and shielding effects of the incident photons by EY [64]. Previous studied showed that pH in dye-sensitized photocatalysis systems could change the existing states of the dye and TEOA as well as the interaction between a dye and a photocatalyst [65], which will then affect H$_2$ evolution rate. As shown in Fig. 6d, the rate of H$_2$ evolution was the highest at its natural pH of 10 and decreased significantly at pH below or above 10. The decrease in the evolution rate at high pH values (> 10) was likely due to the decreased H$^+$ concentration and thermodynamic driving forces for H$_2$ evolution as well as increased electrostatic repulsion forces between deprotonated EY and negatively charged g-C$_3$N$_4$ [66–68]. Lowing the pH value from 10 to 8 led to a dramatic decrease in H$_2$ evolution rate, which can be attributed to the protonation of TEOA, which becomes a less effective electron donor [65].

Stability of CN/FeNi$_{7.47}$P/g-C$_3$N$_4$ was evaluated by performing recycling experiments under visible-light irradiation. At the end of each run, the reaction cell was evacuated three times to remove residual H$_2$ produced during prior experiment, and 0.5 mL TEOA was added prior
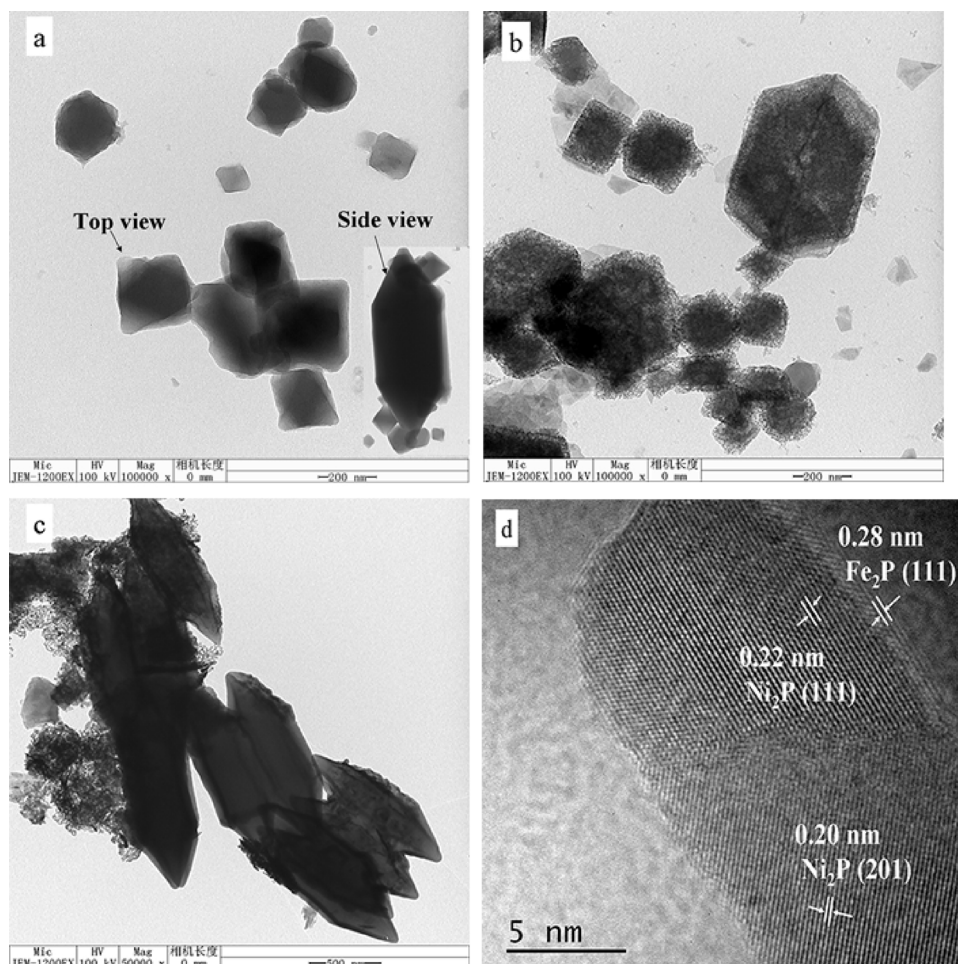
Fig. 3. TEM images of (a) NH$_2$-MIL-101(Fe), (b) NH$_2$-MIL-101(Fe)/Ni(OH)$_2$ and (c) CN/FeNi$_{7.47}$P/g-C$_3$N$_4$ as well as HRTEM image of CN/FeNi$_{7.47}$P/g-C$_3$N$_4$ (d).

to the third, fourth, and fifth evacuation steps. As shown in Fig. 7, no significant decrease in hydrogen evolution amount was observed in five consecutive repeated experiments performed within the 25 h period.

The characteristic peaks of g-C$_3$N$_4$, CN/Fe$_2$P, Ni$_2$P were found in XRD pattern of used CN/FeNi$_{7.47}$P/g-C$_3$N$_4$. Patterns of fresh and used CN/FeNi$_{7.47}$P/g-C$_3$N$_4$ were basically identical (see Fig. S7). XPS also
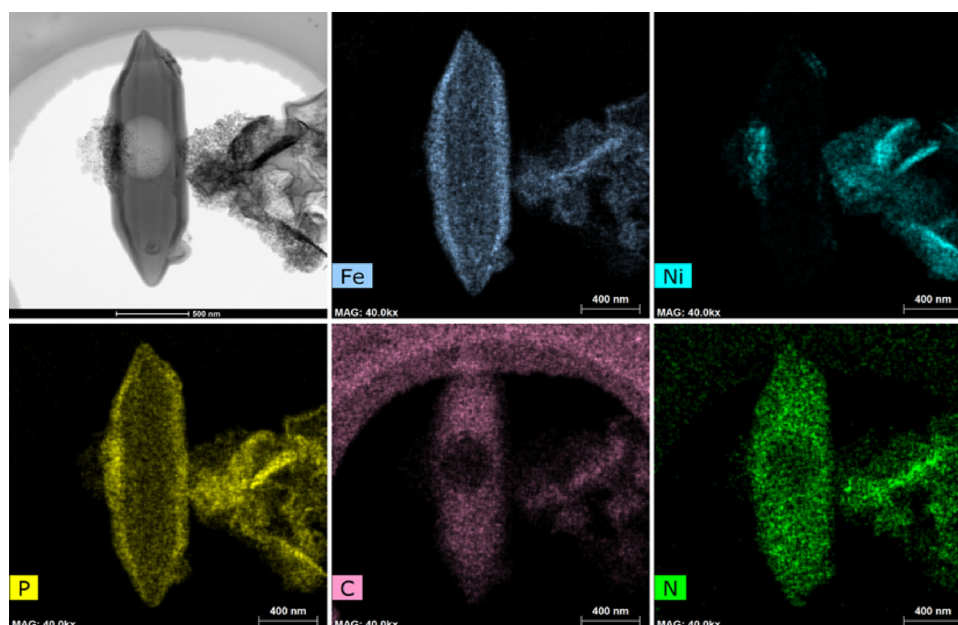

Fig. 4. STEM-EDX images of (a) CN/FeNi$_{7.47}$P/g-C$_3$N$_4$ composite and the corresponding element mapping for (b) Fe, (c) Ni, (d) P, (e) C and (f) N.
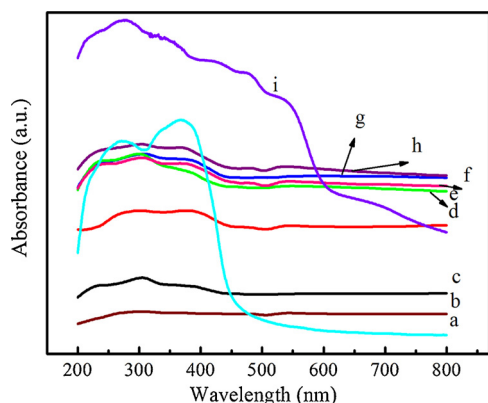
Fig. 5. UV–vis diffuse reflectance spectra of the as-prepared (a) $g-C_3N_4$, (b) CN/Fe_2P, (c) CN/FeP/$g-C_3N_4$, (d) CN/FeNi$_{2.65}$P/$g-C_3N_4$, (e) CN/FeNi$_{4.25}$P/$g-C_3N_4$ (f) CN/FeNi$_{6.71}$P/$g-C_3N_4$, (g) CN/FeNi$_{7.47}$P/$g-C_3N_4$ (h) CN/FeNi$_{11.37}$P/$g-C_3N_4$, and (i) EY.

confirmed existence of the Ni, Fe, and P elements, and no changes in their valence states in the used CN/FeNi$_{7.47}$P/$g-C_3N_4$ composite occurred (Fig. S8). Thus, obtained CN/FeNiP/$g-C_3N_4$ composite has good stability in photocatalytic H_2 evolution from the water splitting.

3.3. Mechanism

The light-induced charge transfer of the as-prepared catalysts can be discussed by analyzing their photoluminescence (PL) emission spectra (Fig. 8a). EY-sensitized $g-C_3N_4$ showed strong PL emission peak centered at ~ 570 nm. Coupling of $g-C_3N_4$ with CN/Fe_2P (CN/FeP/$g-C_3N_4$) weakened its PL peak intensity indicating charge transfer process from EY and $g-C_3N_4$ to CN/Fe_2P. The PL peak intensity further decreased after Ni_2P was incorporated into CN/FeP/$g-C_3N_4$. CN/FeNi$_{7.47}$P/$g-C_3N_4$ showed the lowest PL peak intensity revealing that the combination Ni_2P with Fe_2P as cocatalyst could effectively facilitate the charge transfer and suppress the electron-hole recombination of EY-sensitized $g-C_3N_4$. TRPL spectra shown in Fig. 8b also indicated that the charge

carriers lifetime in the EY-sensitized CN/FeNi$_{7.47}$P/$g-C_3N_4$ composite (2.08 ns) was higher than that in the pure $g-C_3N_4$ (1.01 ns) and CN/FeP/$g-C_3N_4$ (1.39 ns). It was obvious that the charge carriers lifetime of $g-C_3N_4$ was prolonged by decorating it with Fe_2P and Ni_2P, which facilitated more photo-generated electrons participating in the photocatalytic reaction towards H_2 evolution.

The transient photocurrent responses of EY-sensitized $g-C_3N_4$, CN/FeP/$g-C_3N_4$ and CN/FeNi$_{7.47}$P/$g-C_3N_4$ were also analyzed to determine their charge-separation efficiency. As shown in Fig. 9a, $g-C_3N_4$ shows a low photocurrent response. After decorating $g-C_3N_4$ with CN/Fe_2P, photocurrent response was enhanced, and the CN/FeNi$_{7.47}$P/$g-C_3N_4$ composite showed the highest photocurrent indicating the most efficient transfer of charge carriers corresponding to the best photocatalytic activity in the water splitting reaction (Fig. 6). In addition, CN/FeNi$_{7.47}$P/$g-C_3N_4$ exhibited the smallest radius of the electrochemical impedance semi-circle (see Nyquist plots in Fig. 9b) comparing to both $g-C_3N_4$ and CN/FeP/$g-C_3N_4$ further demonstrating that the simultaneous introduction of Fe_2P and Ni_2P promotes efficient transfer of photo-generated electrons.

To further understand how CN/FeNiP improved charge-separation efficiency and photocatalytic hydrogen evolution in the EY-sensitized CN/FeNiP/$g-C_3N_4$ composite, positions of the edge potential of the conduction (E_{CB}) of $g-C_3N_4$, CN/Fe_2P, and Ni_2P were determined. Based on the Tauc plots of $(\alpha h\nu)^2$ vs photon energy ($h\nu$) (shown in Fig. S9d) and UV–vis absorption spectrum (shown in Fig. 5), the band gap (E_g) of $g-C_3N_4$ was calculated to be 2.68 eV. Positive tangent slopes in the MS plots (shown in Fig. S9) revealed that $g-C_3N_4$, CN/Fe_2P and Ni_2P exhibited characteristics typical of n-type semiconductors. The corresponding flat band potentials were −1.18, −1.02, and −1.50 eV versus Ag/AgCl for $g-C_3N_4$, CN/Fe_2P and Ni_2P, respectively. Generally, E_{CB} values for n-type semiconductors are more negative (by about −0.2 eV) than their flat band potentials [24,45,69]. Thus, E_{CB} for $g-C_3N_4$, CN/Fe_2P and Ni_2P are about −1.38, −1.22 and −1.70 eV vs Ag/AgCl, respectively. These values translate into −1.18, −1.02 and −1.50 eV vs normal hydrogen electrode (NHE) ($E_{NHE} = E_{Ag/AgCl} + 0.197$) [70]. The valence bands (E_{VB}) of $g-C_3N_4$ was calculated to be 1.50 eV vs NHE.

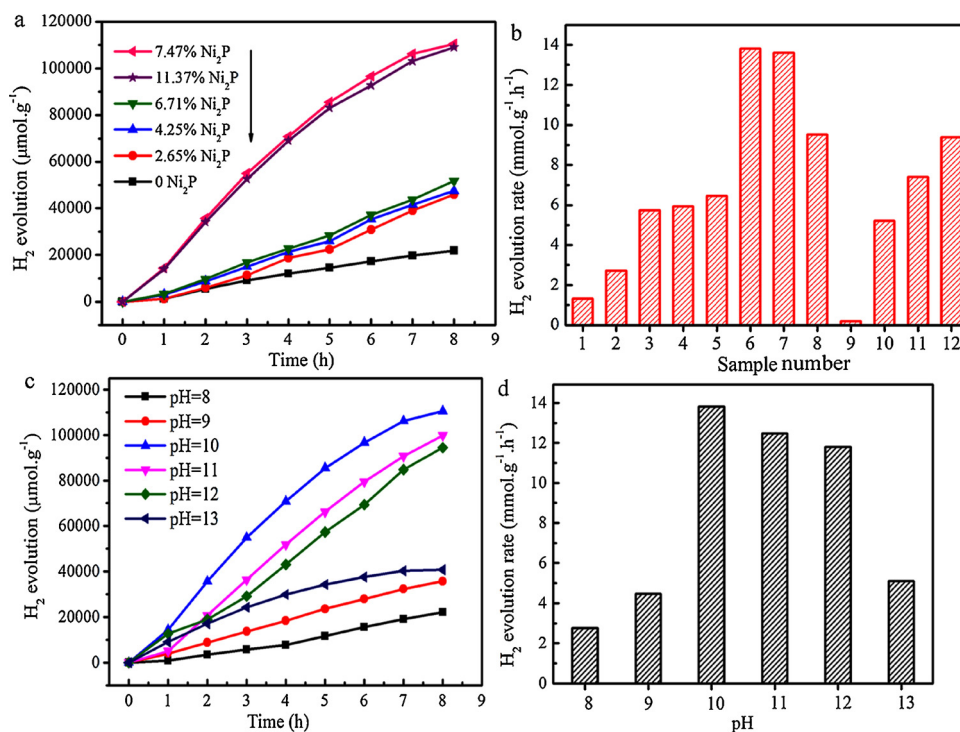Based on above experimental results, the proposed mechanism of

Fig. 6. (a) H_2 amount produced over corresponding photocatalysts and (b) H_2 evolution rates over (1) $g-C_3N_4$, (2) CN/FeP/$g-C_3N_4$, (3) CN/FeNi$_{2.65}$P/$g-C_3N_4$, (4) CN/FeNi$_{4.25}$P/$g-C_3N_4$ (5) CN/FeNi$_{6.71}$P/$g-C_3N_4$, (6) CN/FeNi$_{7.47}$P/$g-C_3N_4$, (7) CN/FeNi$_{11.37}$P/$g-C_3N_4$, (8) physically mixed CN/FeNi$_{7.47}$P + $g-C_3N_4$ as well as over CN/FeNi$_{7.47}$P/$g-C_3N_4$ with various EY concentration (in mmol L^{-1}): (9) 0, (10) 0.1, (11) 0.5, (12) 1.5; (c) and (d) Effects of solution pH on H_2 evolution amount and rate over CN/FeNi$_{7.47}$P/$g-C_3N_4$ composite.

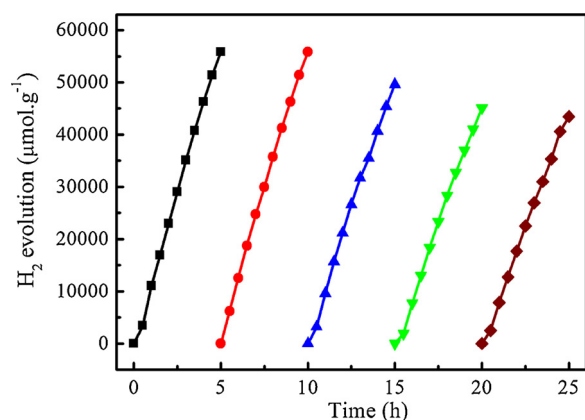**Fig. 7.** Five consecutive experiments measuring amount of H_2 evolved under visible-light irradiation over the same CN/FeNi$_{7.47}$P/g-C$_3$N$_4$ composite cleaned between the experiments.
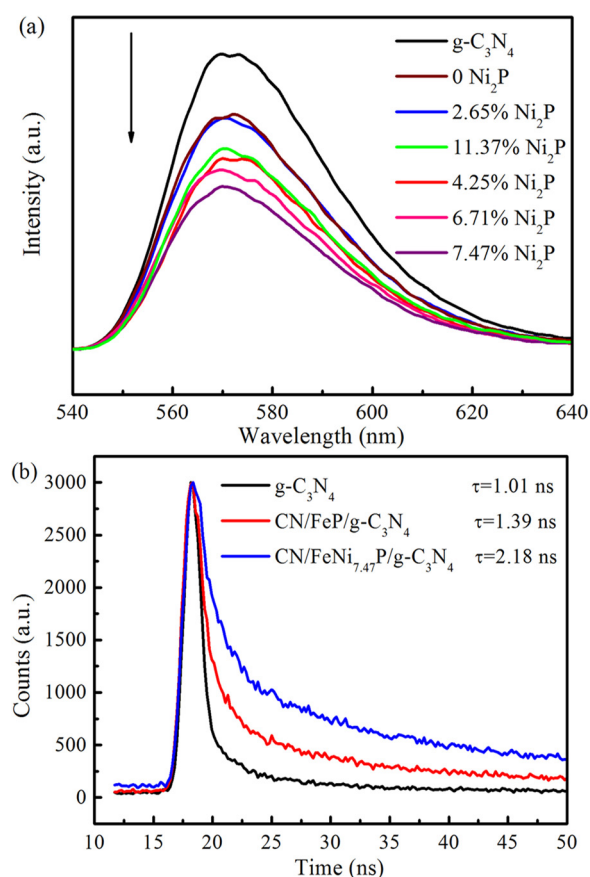

Fig. 8. (a) Photoluminescence spectra of the EY-sensitized g-C$_3$N$_4$ and CN/FeNiP/g-C$_3$N$_4$ with various Ni$_2$P loading amounts; (b) TRPL spectra of EY-sensitized g-C$_3$N$_4$, CN/FeP/g-C$_3$N$_4$ and CN/FeNi$_{7.47}$P/g-C$_3$N$_4$ composites.

Fig. 9. (a) Transient photocurrent responses of the EY-sensitized g-C$_3$N$_4$, CN/FeP/g-C$_3$N$_4$ and CN/FeNi$_{7.47}$P/g-C$_3$N$_4$ at 1.23 V versus RHE. (b) EIS curves of the electrodes composed of g-C$_3$N$_4$, CN/FeP/g-C$_3$N$_4$ and CN/FeNi$_{7.47}$P/g-C$_3$N$_4$ composites.

Scheme 1. Photocatalytic mechanism of H_2 evolution over the EY-sensitized CN/FeNiP/g-C$_3$N$_4$ composite with TEOA as a sacrificial agent under visible-light irradiation.

photocatalytic H_2 evolution by the CN/FeNiP/g-C$_3$N$_4$ composite under visible-light irradiation using EY as a photosensitizer is presented in Scheme 1. Under visible-light illumination, EY and g-C$_3$N$_4$ are easily excited and generate electrons. The HOMO and LUMO levels of EY and EY* are –5.60 and –3.45 eV, respectively [65]. The more negative LUMO level of EY* comparing to the CB levels of g-C$_3$N$_4$, Ni$_2$P and CN/Fe$_2$P is favorable for the photo-generated electrons transport. Therefore, the electrons from EY* can transfer to CB of g-C$_3$N$_4$, Ni$_2$P and CN/Fe$_2$P. Moreover, electrons captured by Ni$_2$P and g-C$_3$N$_4$ or generated by g-C$_3$N$_4$ can transfer to the CN/Fe$_2$P because of its slightly higher E$_{CB}$ comparing to Ni$_2$P and g-C$_3$N$_4$, which helps with charge separation. CB-
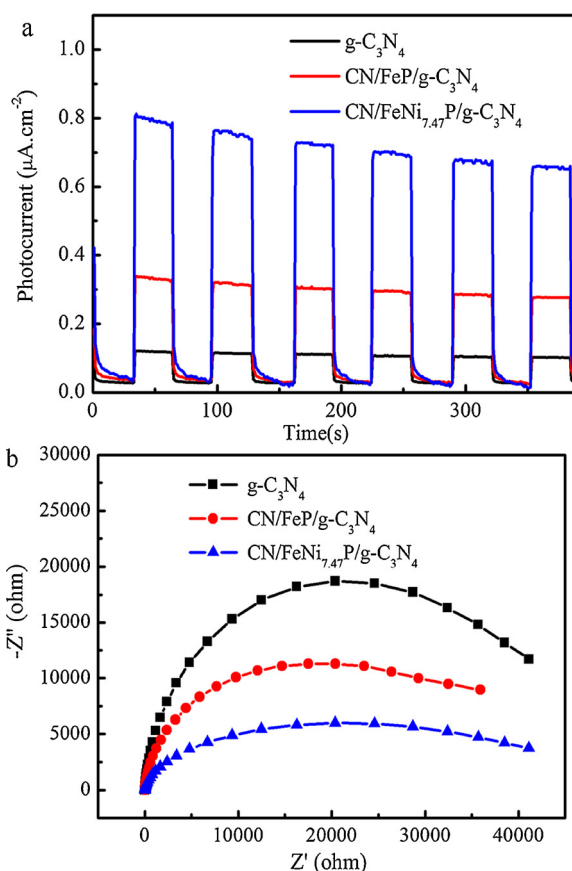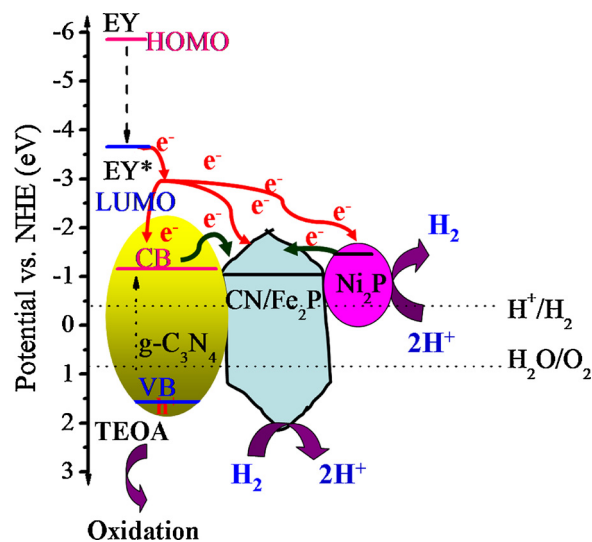
electrons of g-C$_3$N$_4$ together with the electrons accumulated on CN/Fe$_2$P and Ni$_2$P can reduce H$^+$ to produce H_2. Holes in g-C$_3$N$_4$ can be consumed by TEOA because its redox potential (–0.84 eV) is lower than the E$_{VB}$ of g-C$_3$N$_4$ (+ 1.50 eV). During the photocatalytic reaction processes, tight contact between CN/Fe$_2$P, Ni$_2$P and g-C$_3$N$_4$ can act as an electron transport bridge to accelerate the charge transfer, thus,

resulting in enhanced photocatalytic H_2 evolution. Therefore, CN/FeNiP cocatalyst plays the following roles in enhancing H_2 evolution activity of EY-sensitized g-C_3N_4: i) it increases the visible-light absorption intensity of g-C_3N_4; ii) it acts as electron collector to capture electron from excited EY and CB of g-C_3N_4; iii) it suppresses the reverse electron transfer and retards electron-hole recombination; and iv) it serves as an active site to accelerate H_2 evolution.

Control experiment showed a relatively slow H_2 generation rate of $9.52\,mmol\,g^{-1}\,h^{-1}$ over physically mixed CN/FeNiP and g-C_3N_4 in comparison with CN/FeNiP/g-C_3N_4 system, in which H_2 generation rate was $13.81\,mmol\,g^{-1}\,h^{-1}$. Therefore, direct phosphidation of NH_2-MIL-101(Fe) anchored with $Ni(OH)_2$ and g-C_3N_4 has the following advantages in enhancing photocatalytic H_2 production of EY-sensitized g-C_3N_4: i) the NH_2-MIL-101(Fe)-derived CN/FeP can provide more exposed and free surfaces, which can act as reduction reaction active sites; ii) NH_2-MIL-101(Fe) with large specific surface area (equal to $310.8\,m^2/g$) facilitates formation of NH_2-MIL-101(Fe)/g-C_3N_4 heterostructure with tight contact interface; as a result, its CN/FeP/g-C_3N_4 derivative also inherited a close contact interface, which can facilitate charge transport; iii) introduction of Ni_2P can further suppress recombination of photo-induced electrons and holes (according to the TRPL plots) as well as increase visible-light absorption intensity of composites and reduce active sites.

4. Conclusions

CN/FeNiP polyhedron derived from *in situ* phosphidation of NH_2-MIL-101(Fe)/$Ni(OH)_2$ was used as high-efficiency cocatalyst for enhancing photocatalytic H_2 evolution of EY-sensitized g-C_3N_4. Compared to g-C_3N_4 and CN/FeP/g-C_3N_4, CN/FeNi$_{7.47}$P/g-C_3N_4 exhibited the highest photocatalytic activity with a H_2 evolution rate equal to $13.81\,mmol\,g^{-1}\,h^{-1}$ under EY-sensitization. Its apparent quantum yield was 48.5% at 420 nm. The enhanced photocatalytic activity can be attributed to the efficient spatial separation of photo-induced electrons from excited EY and g-C_3N_4 to CN/Fe_2P and Ni_2P owing to their good interface, staggered band energy between g-C_3N_4, CN/Fe_2P and Ni_2P, more surface active sites presented on CN/Fe_2P and promoted H^+ reduction reactions on Ni-Fe phosphides. This work opens new insights on the utilization of MOF-derived hybrid cocatalyst as a substitute for noble metals for effective photocatalytic H_2 production in EY-sensitized system.

Acknowledgements

Appendix A. Supplementary data

Supplementary material related to this article can be found, in the online version, at doi:https://doi.org/10.1016/j.apcatb.2018.09.035.

References

[1] A. Kudo, Y. Miseki, Chem. Soc. Rev. 38 (2009) 253–278.
[2] S.Y. Tee, K.Y. Win, W.S. Teo, L.D. Koh, S.H. Liu, C.P. Teng, M.Y. Han, Adv. Sci. 4 (2017) 1600337–1600360.
[3] Y.J. Yuan, D.Q. Chen, J.S. Zhong, L.X. Yang, J.J. Wang, M.J. Liu, W.G. Tu, Z.T. Yu, Z.G. Zou, J. Mater. Chem. A 5 (2017) 15771–15779.
[4] X.X. Zhao, J.R. Feng, J.W. Liu, J. Lu, W. Shi, G.M. Yang, G.C. Wang, P.Y. Feng, P. Cheng, Adv. Sci. 5 (2018) 1700590–1700598.
[5] D.D. Ma, J.W. Shi, Y.J. Zou, Z.Y. Fan, X. Ji, C.M. Niu, L.Z. Wang, Nano Energy 39 (2017) 183–191.
[6] A. Naseri, M. Samadi, A. Pourjavadi, A.Z. Moshfegh, S. Ramakrishna, J. Mater. Chem. A 5 (2017) 23406–23433.
[7] L.L. Zhao, J. Jia, Z.Y. Yang, J.Y. Yu, A.L. Wang, Y.H. Sang, W.J. Zhou, H. Liu, Appl. Catal. B: Environ. 210 (2017) 290–296.
[8] Y.J. Hao, S.Z. Kang, X. Liu, X.Q. Li, L.X. Qin, J. Mu, ACS Sustain. Chem. Eng. 5 (2017) 1165–1172.
[9] C.Z. Sun, H. Zhang, H. Liu, X.X. Zheng, W.X. Zou, L. Dong, L. Qi, Appl. Catal. B: Environ. 235 (2018) 66–74.
[10] W.N. Xing, W.G. Tu, Z.H. Han, Y.D. Hu, Q.Q. Meng, G. Chen, ACS Energy Lett. 3 (2018) 514–519.
[11] Z.P. Yan, Z.J. Sun, X. Liu, H.X. Jia, P.W. Du, Nanoscale 8 (2016) 4748–4756.
[12] J.J. Ding, X.Y. Li, L. Chen, X. Zhang, S. Sun, J. Bao, C. Gao, X.Y. Tian, J. Mater. Chem. A 4 (2016) 12630–12637.
[13] Y. Lu, X. Cheng, G. Tian, H. Zhao, L. He, J. Hu, S.M. Wu, Y. Dong, G.G. Chang, S. Lenaerts, S. Siffert, G.V. Tendeloo, Z.F. Li, L.L. Xu, X.Y. Yang, B.L. Su, Nano Energy 47 (2018) 8–17.
[14] M.Y. Xing, B.C. Qiu, M.M. Du, Q.H. Zhu, L.Z. Wang, J.L. Zhang, Adv. Funct. Mater. 27 (2017) 1702624–1702633.
[15] Q.Z. Huang, Z.J. Tao, L.Q. Ye, H.C. Yao, Z.J. Li, Appl. Catal. B: Environ. 237 (2018) 689–698.
[16] L.Z. Xu, X.Y. Deng, Z.H. Li, Appl. Catal. B: Environ. 234 (2018) 50–55.
[17] Y.J. Chen, R.K. Huang, D.Q. Chen, Y.S. Wang, W.J. Liu, X.N. Li, Z.H. Li, ACS Appl. Mater. Interfaces 4 (2012) 2273–2279.
[18] H.S. Zhai, X.L. Liu, P. Wang, B.B. Huang, Q.Q. Zhang, Appl. Surf. Sci. 430 (2018) 515–522.
[19] Z.X. Qin, F. Xue, Y.B. Chen, S.H. Shen, L.J. Guo, Appl. Catal. B: Environ. 217 (2017) 551–559.
[20] W.J. Ong, L.L. Tan, Y.H. Ng, S.T. Yong, S.P. Chai, Chem. Rev. 116 (2016) 7159–7329.
[21] X.J. Bai, R.L. Zong, C.X. Li, D. Liu, Y.F. Liu, Y.F. Zhu, Appl. Catal. B: Environ. 147 (2014) 82–91.
[22] J.J. Xue, S.S. Ma, Y.M. Zhou, Z.W. Zhang, M. He, ACS Appl. Mater. Interfaces 7 (2015) 9630–9637.
[23] X.L. Zhang, X.X. Zhang, J.D. Li, J.H. Sun, J. Bian, J.S. Wang, Y. Qu, R. Yan, C.L. Qin, L.Q. Jing, Appl. Catal. B: Environ. 237 (2018) 50–58.
[24] S.S. Yi, J.M. Yan, B.R. Wulan, S.J. Li, K.H. Liu, Q. Jiang, Appl. Catal. B: Environ. 200 (2017) 477–483.
[25] Y. Liang, Q. Liu, A.M. Asiri, X. Sun, Y. Luo, ACS Catal. 4 (2014) 4065–4069.
[26] P. Xiao, M.A. Sk, L.T. Thia, X. Ge, R.J. Lim, J.Y. Wang, K.H. Lim, X. Wang, Energy Environ. Sci. 7 (2014) 2624–2629.
[27] Z.J. Sun, Q.D. Yue, J.S. Li, J. Xu, H.F. Zheng, P.W. Du, J. Mater. Chem. A 3 (2015) 10243–10247.
[28] R.C. Shen, J. Xie, X.Y. Lu, X.B. Chen, X. Li, ACS Sustain. Chem. Eng. 6 (2018) 4026–4036.
[29] Z.Y. Lu, C.M. Li, J. Han, L. Wang, S.H. Wang, L. Ni, Y. Wang, Appl. Catal. B: Environ. 237 (2018) 919–926.
[30] Y.H. Chung, K. Gupta, J.H. Jang, H.S. Park, I. Jang, J.H. Jang, Y.K. Lee, S.C. Lee, S.J. Yoo, Nano Energy 26 (2016) 496–503.
[31] L.M. Song, T.T. Li, S.J. Zhang, S.N. Zhang, Chem. Eng. J. 314 (2017) 498–507.
[32] L. Wei, Y.J. Chen, Y.P. Lin, H.S. Wu, R.S. Yuan, Z.H. Li, Appl. Catal. B: Environ. 144 (2014) 521–527.
[33] Y.D. Hou, Y.S. Zhu, Y. Xu, X.C. Wang, Appl. Catal. B: Environ. 156–157 (2014) 122–127.
[34] Z.Y. Wang, J.W. Peng, X. Feng, Z.X. Ding, Z.H. Li, Catal. Sci. Technol. 7 (2017) 2524–2530.
[35] L. Wei, Y.J. Chen, J.L. Zhao, Z.H. Li, Beilstein J. Nanotechnol. 4 (2013) 949–955.
[36] J. Theerthagiri, R.A. Senthil, B. Senthilkumar, A.R. Polu, J. Madhavan, M. Ashokkumar, J. Solid State Chem. 252 (2017) 43–71.
[37] J.W. Fu, C.B. Bie, B. Cheng, C.J. Jiang, J.G. Yu, ACS Sustain. Chem.. Eng. 6 (2018) 2767–2779.
[38] R.C. Shen, J. Xie, P.Y. Guo, L.S. Chen, X.B. Chen, X. Li, ACS Appl. Energy Mater. 1 (2018) 2232–2241.
[39] H. Zhao, J.W. Wang, Y.M. Dong, P.P. Jiang, ACS Sustain. Chem. Eng. 5 (2017) 8053–8060.
[40] J.F. Callejas, J.M. McEnaney, C.G. Read, J.C. Crompton, A.J. Biacchi, E.J. Popczun, T.R. Gordon, N.S. Lewis, R.E. Schaak, ACS Nano 8 (2014) 11101–11107.
[41] J. Li, J. Lin, Mater. Lett. 221 (2018) 289–292.
[42] Z.W. Pan, R. Wang, J.N. Li, S. Iqbala, W. Liu, K.B. Zhou, Int. J. Hydrogen Energ. 43 (2018) 5337–5345.
[43] X.P. Zhang, L. Huang, Q.Q. Wang, S.J. Dong, J. Mater. Chem. A 5 (2017) 18839–18844.
[44] L.M. Song, S.J. Zhang, J. Ind. Eng. Chem. 61 (2018) 197–205.
[45] Z.X. Qin, Y.B. Chen, Z.X. Huang, J.Z. Su, L.J. Guo, J. Mater. Chem. A 5 (2017) 19025–19035.
[46] L.L. Bi, X.P. Gao, L.J. Zhang, D.J. Wang, X.X. Zou, T.F. Xie, ChemSusChem 11 (2018) 276–284.
[47] P. Li, H.C. Zeng, J. Mater. Chem. A 6 (2018) 2231–2238.
[48] Y.C. Ge, P. Dong, S.R. Craig, P.M. Ajayan, M.X. Ye, J. Shen, Adv. Energy Mater. (2018) 1800484–1800492.
[49] K. Rui, G.Q. Zhao, Y.P. Chen, Y. Lin, Q. Zhou, J.Y. Chen, J.X. Zhu, W.P. Sun, W. Huang, S.X. Dou, Adv. Funct. Mater. (2018) 1801554–1801562.
[50] X.H. Zhang, T.Y. Peng, S.S. Song, J. Mater. Chem. A 4 (2016) 2365–2402.
[51] P. Chowdhury, G. Malekshoar, A.K. Ray, Inorganics 5 (2017) 34–68.
[52] R. Wang, X.Y. Dong, J. Du, J.Y. Zhao, S.Q. Zang, Adv. Mater. 30 (2017) 1703711–1703720.
[53] M.M. Wang, M.T. Lin, J.T. Li, L. Huang, Z.C. Zhuang, C. Lin, L. Zhou, L.Q. Mai, Chem. Commun. 53 (2017) 8372–8375.
[54] D.P. Kumar, J. Choi, S. Hong, D.A. Reddy, S. Lee, T.K. Kim, ACS Sustain. Chem. Eng. 4 (2016) 7158–7166.

[55] X.H. Li, W.L. Guo, Z.H. Liu, R.Q. Wang, H. Liu, J. Hazard. Mater. 324 (2017) 665–672.
[56] J.Q. Wen, J. Xie, X.B. Chen, X. Li, Appl. Surf. Sci. 391 (2017) 72–123.
[57] Y.P. Wang, L.L. Zhang, H.H. Li, Y.J. Wang, L.F. Jiao, H.T. Yuan, L. Chen, H. Tang, X.F. Yang, J. Power Sour. 253 (2014) 360–365.
[58] T.F. Wu, P.F. Wang, J. Qian, Y.H. Ao, C. Wang, J. Hou, Dalton Trans. 46 (2017) 13793–13801.
[59] Y.M. Shi, Y. Xu, S.F. Zhuo, J.F. Zhang, B. Zhang, ACS Appl. Mater. Interfaces 7 (2015) 2376–2384.
[60] L.H. Yao, D. Wei, Y.M. Ni, D.P. Yan, C.W. Hu, Nano Energy 26 (2016) 248–256.
[61] W.J. Wang, T.C. An, G.Y. Li, D.H. Xia, H.J. Zhao, J.C. Yu, P.K. Wong, Appl. Catal. B: Environ. 217 (2017) 570–580.
[62] Z.G. Zhang, X.Y. Li, B.J. Liu, Q.D. Zhao, G.H. Chen, RSC Adv. 6 (2016) 4289–4295.
[63] P. Ye, X.L. Liu, J. Iocozzia, Y.P. Yuan, L.N. Gu, G.S. Xu, Z.Q. Lin, J. Mater. Chem. A 5 (2017) 8493–8498.
[64] S.X. Min, G.X. Lu, J. Phys. Chem. C 116 (2012) 25415–25424.
[65] S.X. Min, G.X. Lu, J. Phys. Chem. C 115 (2011) 13938–13945.
[66] X.J. Zhang, Z.L. Jin, Y.X. Li, S.B. Li, G.X. Lu, J. Phys. Chem. C 113 (2009) 2630–2635.
[67] T. Lazarides, T. McCormick, P.W. Du, G.G. Luo, B. Lindley, R. Eisenberg, J. Am. Chem. Soc. 131 (2009) 9192–9194.
[68] D. Li, M.B. Müller, S. Gilje, R.B. Kaner, G.G. Wallace, Nat. Nanotechnol. 3 (2008) 101–105.
[69] X. Li, J.G. Yu, J.X. Low, Y.P. Fang, J. Xiao, X.B. Chen, J. Mater. Chem. A 3 (2015) 2485–2534.
[70] G.J. Ai, H.X. Li, S.P. Liu, R. Mo, J.X. Zhong, Adv. Funct. Mater. 25 (2015) 5706–5713.